Probing nuclear dynamics of oriented HeH^+ with odd-even high-order harmonics

W. Y. Li,[1,2,3] S. J. Yu,[1] S. Wang,[1] and Y. J. Chen[1,*]

[1]*College of Physics and Information Technology, Shaan'xi Normal University, Xi'an, China*

[2]*School of Mathematics and Science, Hebei GEO University, Shijiazhuang, China*

[3]*College of Physics and Information Engineering, Hebei Normal University, Shijiazhuang, China*

(Received 5 April 2016; revised manuscript received 28 September 2016; published 9 November 2016)

We study the electron-nuclear coupled dynamics for oriented HeH^+ molecules in strong laser fields numerically and analytically. At small orientation angles, the asymmetric molecule tends to stretch to distances larger than the equilibrium separation and strong even harmonics are emitted. We show that the permanent dipole of the system plays an important role in the vibrational dynamics of the nuclear wave packet. The nuclear motion and the molecular structure can be read from the spectra and ellipticity of odd-even high harmonics. Our results also have implications for strong-field ionization of the asymmetric system.

DOI: 10.1103/PhysRevA.94.053407

I. INTRODUCTION

In recent years, the development of the laser technology has allowed one to probe the ultrafast dynamics of atoms and molecules on the attosecond time scale [1,2]. These exquisite approaches in ultrafast measurement generally utilize the processes of strong-field ionization [3,4] and high harmonic generation (HHG) [5,6]. The latter has been termed as high harmonic spectroscopy (HHS). The HHS has been used for probing the structure [7–9] and electronic dynamics [10,11] of atoms and molecules in atomic time-space scale. It can also be used to trace the nuclear motion on a subfemtosecond time scale [12,13] and monitor the change of the molecular bond length in a chemical reaction [14].

Recently, there is an increasing interest [15] in the HHS for asymmetric molecules which are active in many chemical processes. For oriented asymmetric molecules, due to symmetry breaking, both odd and even harmonics are emitted, which show different spectral properties [16–18] and carry different information of the target [19–21]. The odd-even HHS already shows promise for use in imaging the asymmetric orbital and revealing the electronic dynamics under the influence of the asymmetric potential [22–25]. On the other hand, with a permanent dipole, the asymmetric molecule shows some complex responses to strong laser fields, such as asymmetric ionization [26] and the large Stark shift [27]. Considering the complex effects, further study on the correlated electron-nuclear dynamics of the oriented asymmetric system is a challenging work in theories and experiments.

In this paper, we extend the theoretical study of odd-even HHS to the vibrating asymmetric system in strong few-cycle laser pulses. The study on vibrating HeH^{2+} has shown that the nuclear motion affects importantly on the HHG [28]. Here, we choose HeH^+ [29], a fundamental benchmark as the simplest heteronuclear ion isoelectronic to H_2 with $X^1\Sigma^+$ symmetry, as the target molecule. We solve the time-dependent Schrodinger equation (TDSE) for oriented HeH^+ in a non-Born-Oppenheimer (non-BO) approach numerically. Our main results are twofold. (1) The asymmetric molecule tends to expand to larger internuclear distances at small orientation angles θ (θ, the angle between the molecular axis and the laser polarization) and stay near its equilibrium geometry at large angles. We show that the permanent dipole of the system, inherent for polar molecules, influences importantly on the nuclear dynamics. (2) Strong even harmonics are observed from the system. We show that the odd-even HHG spectra encode the information of the vibrational dynamics of the asymmetric molecule. The polarization measurement of odd-even HHG also allows one to probe the instantaneous structure of the molecule.

The main results are obtained with a single-active-electron approximation and assuming perfect orientation of the asymmetric system. To check our results, we also simulate the dynamics of the vibrating HeH^+ system with the use of a simple two-electron model, and consider incomplete orientation of the asymmetric system in the paper. The HHG from the vibrating HeH^+ system show some complex phenomena. To understand these phenomena, a comparison study is also performed with exploring the HHG from the vibrating H_2.

II. NUMERICAL PROCEDURE

To describe the coupled electronic and nuclear wave-packet dynamics and consider the orientation effect, we use a non-BO model of HeH^+ with two-dimensional (2D) electron dynamics and one-dimensional (1D) nuclear dynamics. To make the computational effort manageable, a single-active-electron model is also used. The orientation θ of the molecule relative to the field is held fixed since the rotational motion is negligible on the few-cycle time scale ($\sim$10 fs). These treatments are similar to those used for H_2 in [12]. The effective Hamiltonian used here is [30] (atomic units are used throughout)

$$H(t) = H_0 + V(t), \tag{1}$$

where

$$H_0 = T_n + T_e + V_{\text{eff}}(R,\mathbf{r}) \tag{2}$$

is the field-free Hamiltonian with the nuclear kinetic energy operator T_n, the electronic kinetic energy operator T_e, and the effective potential V_{eff} which describes the interaction between

*chenyjhb@gmail.com

the active electron and the nuclei [12]. These terms have the following forms:

$$T_n = -\frac{1}{2\mu_n}\frac{\partial^2}{\partial R^2}, \tag{3}$$

$$T_e = -\frac{1}{2\mu_e}\frac{\partial^2}{\partial \mathbf{r}^2} = -\frac{1}{2\mu_e}\left[\frac{\partial^2}{\partial x^2} + \frac{\partial^2}{\partial y^2}\right], \tag{4}$$

$$V_{\rm eff}(R,\mathbf{r}) = V_{\rm BO}^{+}(R) - \sum_{j=1,2}\frac{Z(R,|\mathbf{r}-\mathbf{R}_j|)}{\sqrt{\xi + |\mathbf{r}-\mathbf{R}_j|^2}}. \tag{5}$$

Here, R is the internuclear separation and $\mathbf{r}$ is the electronic coordinate with respect to the nuclear center of mass. $\mu_n = M_{\rm He}M_{\rm H}/(M_{\rm He}+M_{\rm H})$ is the nuclear reduced mass, and $\mu_e = (M_{\rm He}+M_{\rm H})/(M_{\rm He}+M_{\rm H}+1)$ is the electronic reduced mass. $M_{\rm He}$ and $M_{\rm H}$ are masses of He and H nuclei.

In Eq. (5), the term $V_{\rm BO}^{+}(R)$ denotes the lowest BO potential of HeH^{2+} and

$$Z(R,r_j) = Z_{ji}\exp\left[-\rho(R)r_j^2\right] + Z_{jo} \tag{6}$$

with $r_j = |\mathbf{r}-\mathbf{R}_j| = \sqrt{(x-x_j)^2+(y-y_j)^2}$ and $j = 1,2$. Here, Z_1 and Z_2 are the effective charges for the He and H centers, respectively. The indices i and o denote the inner and outer limits of Z_1 and Z_2. $\mathbf{R}_1$ and $\mathbf{R}_2$ are the positions of the He and H nuclei that have the coordinates of (x_1,y_1) and (x_2,y_2) in the xy plane. These relevant values are $x_{1/2} = \pm R_{1/2}\cos\theta$, $y_{1/2} = \pm R_{1/2}\sin\theta$ with $R_1 = M_{\rm H}R/(M_{\rm He}+M_{\rm H})$ and $R_2 = M_{\rm He}R/(M_{\rm He}+M_{\rm H})$. For HeH^{+}, we have used the parameters of $Z_{1i} = \frac{2}{3}$, $Z_{2i} = \frac{1}{3}$, $Z_{1o} = \frac{4}{3}$, and $Z_{2o} = \frac{2}{3}$. $\xi = 0.5$ is the softening parameter. $\rho(R)$ is the screening parameter, which is adjusted such that the resulting lowest BO potential of the model molecule matches the real HeH^{+} BO potential taken from [31].

In Eq. (1), the term $V(t)$ describes the interaction of the HeH^{+} system and the laser field. The latter used here is $\mathbf{E}(t) = \vec{\mathbf{e}}E(t) = \vec{\mathbf{e}}f(t)E_0\sin\omega_0 t$ with the amplitude E_0, the frequency ω_0, and the envelope function $f(t)$. The symbol $\vec{\mathbf{e}}$ denotes the unit vector along the laser polarization, which is along the x axis here. A sketch of the coordinate system used in our simulations is presented in Fig. 1. In the dipole approximation and the length gauge, the term $V(t)$ in our calculations has the following form [30]:

$$V(t) = V_e(\mathbf{r},t) + V_n(R,t) = xE(t) - \zeta RE(t)\cos\theta, \tag{7}$$

with $\zeta = (aM_{\rm H} - bM_{\rm He})/(M_{\rm He}+M_{\rm H})$. a and b are the charges of He($Z=2$) and H($Z=1$) nuclei, respectively. Considering the respective mass of He (including two protons and two neutrons) and H (including one proton), the value of ζ is $-\frac{2}{5}$. The first term $V_e(\mathbf{r},t) = xE(t)$ in Eq. (7) describes the laser-electron interaction. The second term $V_n(R,t) = -\zeta RE(t)\cos\theta$ describes the laser-nuclei interaction.

In our simulations, we use an eight-cycle laser pulse which is linearly turned on and off for two optical cycles, and then kept at a constant intensity for four additional cycles. The TDSE of $i\dot{\psi}(R,\mathbf{r},t) = H(t)\psi(R,\mathbf{r},t)$ is solved numerically using the spectral method [32]. A grid size of $Lx \times Ly = 204.8 \times 51.2$ a.u. for the electron and a range of $R = 0.6\ldots6.9$ a.u. for the internuclear distance have proven sufficient for converged HHG spectra. Unless mentioned elsewhere, the laser intensity explored here is $I = 2.5\times10^{15}$ W/cm^2, and the laser wavelength is $\lambda = 600$ nm.

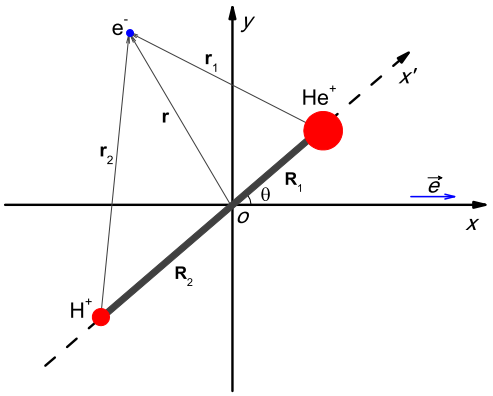

FIG. 1. A sketch of the molecular geometry and the coordinate system used in our simulations. The polarization direction $\vec{\mathbf{e}}$ of the laser field is along the x axis. The molecular axis x' is located in the xy plane with an angle θ to the x axis. The center of mass of the molecular system is located at the origin of the coordinate system o. $\mathbf{R}_1$ and $\mathbf{R}_2$ denote the positions of the two nuclei of He^{+} and H^{+} to the origin, respectively. $\mathbf{r}_1$ and $\mathbf{r}_2$ denote the positions of the electron to these two nuclei and $\mathbf{r}$ denotes that to the origin.

Before discussing our results, we analyze the influence of the term $V_n(R,t)$ of Eq. (7) on the nuclear dynamics. Clearly, the absolute value of the term $V_n(R,t)$ is maximal for $\theta = 0^\circ$ and it decreases with the increase of the angle θ. For $\theta = 90^\circ$, this term disappears. These analyses imply that the laser field plays a more important role in the motion of the nuclei for smaller angles. However, for the laser parameters explored in the paper, the calculated HHG spectra with and without this term at $\theta = 0^\circ$ are very similar to each other (see Fig. 2). We therefore expect that this term $V_n(R,t)$ plays a small role in the nuclear dynamics of the HeH^{+} system. In the following discussions on electron-nuclei coupled dynamics of the asymmetric system, we omit the influence of this term.

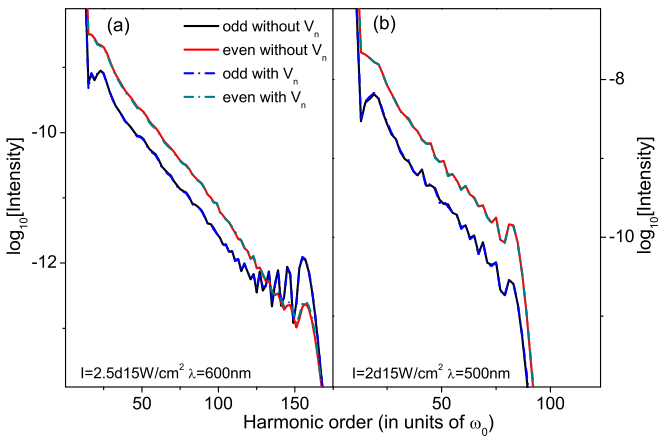

FIG. 2. Comparison of odd-even harmonic spectra of HeH^{+} at $\theta = 0^\circ$, calculated without (solid line) and with (dashed-dotted line) the laser-nuclei-interaction term $V_n(R,t)$ for $I = 2.5\times10^{15}$ W/cm^2 and $\lambda = 600$ nm (a) and $I = 2\times10^{15}$ W/cm^2 and $\lambda = 500$ nm (b).

It should also be noted that the 1D nuclear model used here is applicable only for short pulses. For long ones, the rotational motion of the nuclei can not be neglected and higher dimensions of the nuclear motion need to be considered. In addition, for very intense laser fields, the laser-nuclei-interaction term can also affect the motion of the nuclei and induce the deviation of the nuclear motion from the x' axis (see Fig. 1), especially for intermediate angles θ.

III. NUCLEAR DYNAMICS

A. Evolution of vibrational states

Figure 3 plots the populations of the first vibrational states $\chi_g^{\upsilon}(R)\phi_g(R,\mathbf{r})$ of the HeH^+ system with $\upsilon = 0,1,2\ldots$ at $\theta = 0^\circ$ and 90°. Here, $\phi_g(R,\mathbf{r})$ is the electronic ground-state BO wave function and $\chi_g^{\upsilon}(R)$ is the vibrational wave function associated with $\phi_g(R,\mathbf{r})$. At the frame of BO approximation with R as a parameter, the BO wave function $\phi_g(R,\mathbf{r})$ and the BO potential $V_g(R)$ associated with $\phi_g(R,\mathbf{r})$ can be obtained through imaginary-time propagation of the Hamiltonian

$$H_0^e(R,\mathbf{r}) = T_e + V_{\text{eff}}(R,\mathbf{r}). \tag{8}$$

With diagonalizing the nuclear Hamiltonian

$$H_0^g(R) = T_n + V_g(R), \tag{9}$$

we then can obtain the vibrational eigenstates $\chi_g^{\upsilon}(R)$ and eigenenergy E_g^{υ} associated with $\phi_g(R,\mathbf{r})$. Here, E_g^{υ} is also the energy of the whole Hamiltonian H_0 of Eq. (2) including electronic and nuclear motions. Alternatively, one can obtain $\chi_g^{\upsilon}(R)$ and E_g^{υ} through imaginary-time propagation of the Hamiltonian H_0. Both approaches give results very similar to each other.

One can observe from Fig. 3(a) that for $\theta = 0^\circ$, the population of the ground state $|0\rangle = \chi_g^{\upsilon=0}(R)\phi_g(R,r)$ (bold black curve) decreases very rapidly, as that of the first excited state $|1\rangle = \chi_g^{\upsilon=1}(R)\phi_g(R,r)$ (thin red curve) shows a large population at $t > 1.5T$. T is the laser cycle. This quick depletion of the $|0\rangle$ state disappears for the case of $\theta = 90^\circ$ in Fig. 3(b). In addition, the depletion of the $|0\rangle$ state at $\theta = 0^\circ$ is also asymmetric in one laser cycle. For example,

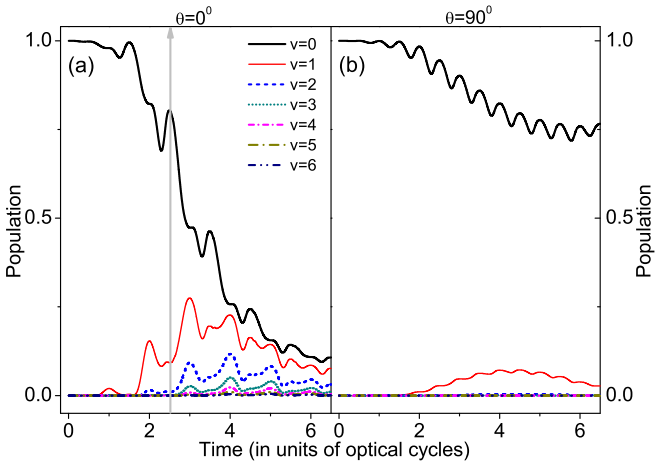

FIG. 3. Time-dependent populations of the first vibrational states of HeH^+ at $\theta = 0^\circ$ (a) and $\theta = 90^\circ$ (b).

around $t = 2.5T$ (the vertical arrow), the bold solid curve falls very fast at $2.5T < t < 3T$ (for which the laser polarization is parallel to the permanent dipole of the system in our simulations), and it almost does not change at $2T < t < 2.5T$ (the antiparallel case). Note, this phenomenon is very different from the fixed-nuclei case of HeH^{2+} in which the depletion of the ground state is more remarkable for the antiparallel case [33].

These above results imply a complex response of the vibrating HeH^+ to the laser field. The simulations with the use of a 1D two-electron model in a non-BO approach for HeH^+, similar to the treatment for 1D H_2 in [34], still reproduce this quick-asymmetric-depletion phenomenon, implying that the latter is related to single-electron dynamics (see Sec. V A).

Aside from the first excited state, other excited states such as $\upsilon = 2$ in Fig. 3(a) of $\theta = 0^\circ$ also show a larger amplitude. On the whole, the amplitudes of the excited states decrease fast as the value of υ increases. However, the structures of the excited-state curves are similar here, implying a similar mechanism for the dynamical evolution of the excited vibrational states. By contrast, the excited states show a small population in Fig. 3(b) of $\theta = 90^\circ$.

B. Effects of permanent dipole

Next, we explore the mechanism for this quick-asymmetric depletion of the $|0\rangle$ state at $\theta = 0^\circ$ with a two-level vibrational model. Let us consider these two lowest states $|0\rangle$ and $|1\rangle$ which have large amplitudes. Under two-level approximations with $\psi(R,\mathbf{r},t) = a_g^0(t)|0\rangle + a_g^1(t)|1\rangle$, we have

$$\begin{aligned} i\dot{a}_g^0(t) &= a_g^0(t)[E_0 + \mathbf{E}(t)\cdot\langle 0|\mathbf{r}|0\rangle] + a_g^1(t)[\mathbf{E}(t)\cdot\langle 0|\mathbf{r}|1\rangle]; \\ i\dot{a}_g^1(t) &= a_g^1(t)\big[E_1 + \mathbf{E}(t)\cdot\langle 1|\mathbf{r}|1\rangle\big] + a_g^0(t)[\mathbf{E}(t)\cdot\langle 1|\mathbf{r}|0\rangle]. \end{aligned} \tag{10}$$

Here, the dipole terms $\langle 0(1)|\mathbf{r}|0(1)\rangle$ and $\langle 0(1)|\mathbf{r}|1(0)\rangle$ are defined as

$$\begin{aligned} \langle m|\mathbf{r}|m\rangle &= \int \big|\chi_g^m(R)\big|^2 \mathbf{D}_p(R)\,dR, \\ \langle m|\mathbf{r}|n\rangle &= \int \big[\chi_g^m(R)\big]^* \chi_g^n(R)\mathbf{D}_p(R)\,dR, \end{aligned} \tag{11}$$

respectively. In Eq. (11), the term

$$\mathbf{D}_p(R) = \int |\phi_g(R,\mathbf{r})|^2 \mathbf{r}\,d\mathbf{r} \tag{12}$$

is the permanent dipole associated with $\phi_g(R,\mathbf{r})$. The above two-level model tells that for $\theta = 0^\circ$ with $E(t)\cdot\mathbf{D}_p(R) \neq 0$, the HeH^+ system initially in the $|0\rangle$ state will be coupled to the $|1\rangle$ state due to the effect of the permanent dipole. In addition, the energy $E_{0(1)}$ of the $|0(1)\rangle$ state will also be dressed strongly by the laser field. This Stark effect is stronger for the $|1\rangle$ state because the value of $\langle 1|\mathbf{r}|1\rangle$ is somewhat larger than that of $\langle 0|\mathbf{r}|0\rangle$. Both of these two states are dressed up (as the laser polarization is antiparallel to the permanent dipole) or down (parallel) simultaneously. As they are dressed down, the energy gap between the two laser-dressed states $|0'\rangle$ and $|1'\rangle$ is smaller and a strong coupling can occur, as shown in Fig. 4. This strong coupling then transfers the population from the ground state

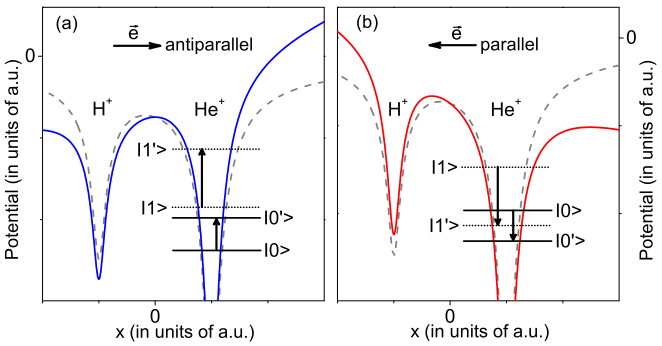

FIG. 4. The schematic of these two lowest vibrational states $|0\rangle$ and $|1\rangle$ dressed by the laser field as the laser polarization is antiparallel (a) and parallel (b) to the permanent dipole. The latter is along the molecular axis (the x axis here) and is directing from the He nucleus to the H nucleus. The field-free (dashed curves) and the laser-dressed (solid curves) potentials of HeH^+ are also shown. See the text for details.

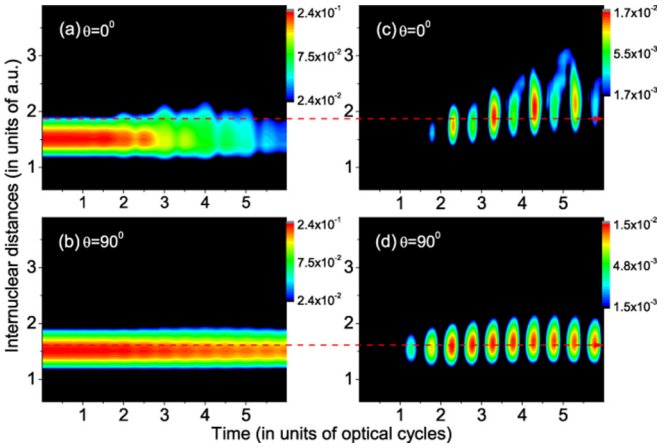

FIG. 5. R-time-dependent distributions $\eta(R,t)$ of bound wave packet $\psi_g(R,\mathbf{r},t)$ (a), (b) and $\alpha(R,t)$ of rescattering wave packet $\psi_{re}(R,\mathbf{r},t)$ (c), (d) at $\theta = 0^\circ$ and 90°.

to the first excited state. The above mechanism, associated with the permanent-dipole effect, for the population transfer between $|0\rangle$ and $|1\rangle$ is also applicable for that between $|0\rangle$ and a higher vibrational state such as $|2\rangle = \chi_g^{v=2}(R)\phi_g(R,r)$, resulting in a high population of the higher state. Due to the similar population-transfer mechanism, the evolution curves of the excited states in Fig. 3(a) also show a similar profile (similar population "dips" and "humps").

Note, for $\theta = 90^\circ$, one arrives at $E(t)\cdot\mathbf{D}_p(R) \equiv 0$ and for symmetric molecules, that is, $\mathbf{D}_p(R) \equiv 0$. For these cases, the two-level model tells that these two lowest states do not couple, in agreement with our TDSE results. The population-transfer mechanism discussed above is somewhat similar to that introduced in [35,36] for H_2^+, where Raman-type processes associated with multiphoton transitions between laser-dressed (but not necessarily adjacent) vibrational states play an important role. Considering the asymmetric depletion of the ground state for the HeH^+ system, we expect that the effect of the permanent dipole is mainly responsible for the phenomenon. This effect is absent for symmetric molecules such as H_2^+ or H_2.

C. Quick nuclear motion

Due to the strong coupling of the lower vibrational states, the initial nuclear wave packet $\chi_g^0(R)$ of the system tends to rapidly spread to larger R, as seen in Fig. 5(a), where we plot the distribution of $\eta(R,t)$ at $\theta = 0^\circ$. The latter is defined as

$$\eta(R,t) = \int |\psi_g(R,\mathbf{r},t)|^2 d\mathbf{r} \tag{13}$$

with

$$\psi_g(R,\mathbf{r},t) = a_g(R,t)\phi_g(R,\mathbf{r}), \tag{14}$$

$$a_g(R,t) = \langle\phi_g(R,\mathbf{r})|\psi(R,\mathbf{r},t)\rangle. \tag{15}$$

The function $\psi_g(R,\mathbf{r},t)$ shown above is the bound wave packet associated with $\phi_g(R,\mathbf{r})$. The amplitude $a_g(R,t)$ describes the dynamical evolution of the nuclear wave packet related to $\phi_g(R,\mathbf{r})$. For $t > 3T$, the distribution in Fig. 5(a) has large amplitudes at distances larger than the equilibrium separation $R_e = 1.5$ a.u. [evaluated from $\chi_g^0(R)$]. By comparison, the distribution $\eta(R,t)$ has large amplitudes around R_e for $\theta = 90^\circ$ in Fig. 5(b). The HHG mainly occurs as the rescattering electron transits back to the ground state $\phi_g(R,\mathbf{r})$ [7,12]. For HeH^+, the above results imply that besides the $\chi_g^0(R)$ state, higher vibrational states $\chi_g^v(R)$ can be involved in the HHG. Next, we turn to the dynamics of the rescattering electron, the recombination of which probes the state of the parent ions.

IV. ELECTRONIC DYNAMICS

A. Spreading of rescattering wave packet

The rescattering wave packet $\psi_{re}(R,\mathbf{r},t)$ has been shown to include full dynamical information of the rescattering electron. It can be obtained numerically following the procedure introduced in [37]. That is,

$$\psi_{re}(R,\mathbf{r},t) = f(r,r_c)\psi_c(R,\mathbf{r},t), \tag{16}$$

where

$$f(r,r_c) = 1 \ \ (r = |\mathbf{r}| < r_c),$$
$$f(r,r_c) = \exp[-(r-r_c)^2/\triangle^2] \ \ (r \geqslant r_c)$$

with $r_c = 10$ a.u. and $\triangle = 2$. The function $\psi_c(R,\mathbf{r},t)$ appearing in Eq. (16) is the continuum wave packet. Here, it can be approximately evaluated with excluding the components of the two lowest electronic BO bound states $\phi_g(R,r)$ and $\phi_f(R,r)$ from $\psi(R,\mathbf{r},t)$. Results obtained with excluding more bound states are similar to those with this above treatment. Figure 6 plots the R-dependent distribution $\zeta(R)$ of the rescattering wave packet at different angles, which is defined as

$$\zeta(R) = \frac{\int |\psi_{re}(R,\mathbf{r},t)|^2 d\mathbf{r}\, dt}{\int |\psi_{re}(R,\mathbf{r},t)|^2 dR\, d\mathbf{r}\, dt}. \tag{17}$$

It is clear, the distribution $\zeta(R)$ shows a single peak with its maximum at a distance $R_m = 1.9$ a.u. for $\theta = 0^\circ$. This peak shifts to smaller R as the angle increases. For $\theta = 90^\circ$, the maximum is located at $R_m = 1.6$ a.u. (near to the equilibrium

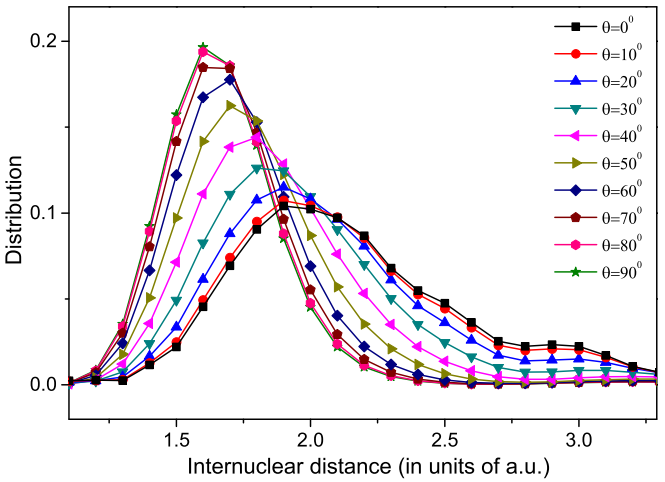

FIG. 6. R-dependent distributions $\zeta(R)$ of rescattering wave packet $\psi_{re}(R,\mathbf{r},t)$ at different angles θ.

distance R_e). The distance R_m corresponding to the peak of the distribution $\zeta(R)$ at an angle θ is expected to play an important role in the HHG of the asymmetric system. We will return to the point later. In Figs. 5(c) and 5(d), we also show the R-time-dependent distributions $\alpha(R,t)$ at different angles. That is,

$$\alpha(R,t) = \int |\psi_{re}(R,\mathbf{r},t)|^2 d\mathbf{r}. \tag{18}$$

One can observe that the distribution in Fig. 5(c) differs remarkably from that in Fig. 5(d). The former shows a more complicated time-dependent structure (which is believed to be related to the effect of the permanent dipole [26,27]) and spans a wider range of R.

Comparisons between the corresponding rescattering and bound distributions in Fig. 5 provide deep insights into the HHG of the vibrating system. For $\theta = 0^\circ$ in Figs. 5(a) and 5(c), one can observe that as the time increases, both bound and rescattering distributions expand towards larger R. In particular, as the bound distribution spreads to $R = 1.9$ a.u., the rescattering one also has large amplitudes around $R = 1.9$ a.u., as indicated by the dashed arrow. For $\theta = 90^\circ$ in Figs. 5(b) and 5(d), both distributions concentrate around R_e. These phenomena can be understood as follows. Tunneling ionization of the bound electron is usually easier to occur at larger R [38,39]. If we assume that the nuclear wave packet related to $\phi_g(R,\mathbf{r})$ spreads to a distance R_m around which the ionization predominantly occurs, the rescattering wave packet arising from tunneling will also have large amplitudes around the distance R_m [the value of R_m read from Fig. 6 therefore can be considered as the spreading extent of the nuclear wave packet of $\phi_g(R,\mathbf{r})$]. The spread of the nuclear wave packet differs for different angles, resulting in the angle-dependent behaviors of the distributions in Fig. 5. Because the HHG intensity depends on the overlap of the rescattering and bound wave packets [7,12], one can expect that the HHG will mainly occur around the distance R_m.

It should be stressed that the variable R_m has a certain value for an angle θ. The function $\zeta(R)$ defined in Eq. (17) has the maximal value at a distance R_m for an angle θ. One therefore can abstract the values of R_m from the function curves of $\zeta(R)$ for different angles in Fig. 6. The HHG mechanism of the system associated with R_m is further explored below.

B. Odd-even HHG

In Fig. 7, we show the odd-even HHG spectra parallel to the laser polarization at different angles θ, which have been divided by the corresponding ionization probability for comparison. The coherent part of the spectra parallel or perpendicular to the laser polarization can be evaluated using [40]

$$F_{\parallel(\perp)}(\omega) = \int \langle\psi(t)|\vec{\mathbf{e}}_{\parallel(\perp)}\cdot\nabla_{\mathbf{r}}V_{\rm eff}|\psi(t)\rangle e^{i\omega t}dt, \tag{19}$$

where $\vec{\mathbf{e}}_{\parallel(\perp)}$ is the unit vector parallel (perpendicular) to the laser polarization and $\psi(t) \equiv \psi(R,\mathbf{r},t)$. We also compare the spectra to relevant odd (even) dipoles $D_{\rm odd\,(even)}(\omega,\theta)$, which are mainly responsible for the emission of odd (even) harmonics ω, as introduced in [19,25]. Assuming that the electronic ground-state wave function of the asymmetric molecule in BO approximation has the form of $\phi_g(R,\mathbf{r}) = N_f(a_1e^{-\kappa r_a} + a_2e^{-\kappa r_b})$ and approximating the continuum state $|\mathbf{p}\rangle$ using the plane wave, the dipole $D_{\rm odd} \equiv D_{\rm odd}(\omega,\theta)$ which is mainly responsible for the emission of odd harmonics along the laser polarization $\vec{\mathbf{e}}_{\parallel}$ can be written as

$$D_{\rm odd}(\omega,\theta) \propto G_{\rm odd}(\omega,\theta)\int d\mathbf{r}[e^{-\kappa r}\vec{\mathbf{e}}_{\parallel}\cdot\mathbf{r}\sin(\mathbf{p}_k\cdot\mathbf{r})], \tag{20}$$

with $G_{\rm odd}(\omega,\theta) = a_1\cos(p_kR_1\cos\theta) + a_2\cos(p_kR_2\cos\theta)$. Similarly, the dipole $D_{\rm even} \equiv D_{\rm even}(\omega,\theta)$ which is related to the emission of even harmonics along the laser polarization, can be written as

$$D_{\rm even}(\omega,\theta) \propto G_{\rm even}(\omega,\theta)\int d\mathbf{r}[e^{-\kappa r}\vec{\mathbf{e}}_{\parallel}\cdot\mathbf{r}\sin(\mathbf{p}_k\cdot\mathbf{r})], \tag{21}$$

with $G_{\rm even}(\omega,\theta) = a_1\sin(p_kR_1\cos\theta) - a_2\sin(p_kR_2\cos\theta)$. Here, $a_1 = Z_1/B$, $a_2 = Z_2/B$, $B = (Z_1^2+Z_2^2)^{1/2}$, $r_a = |\mathbf{r}$

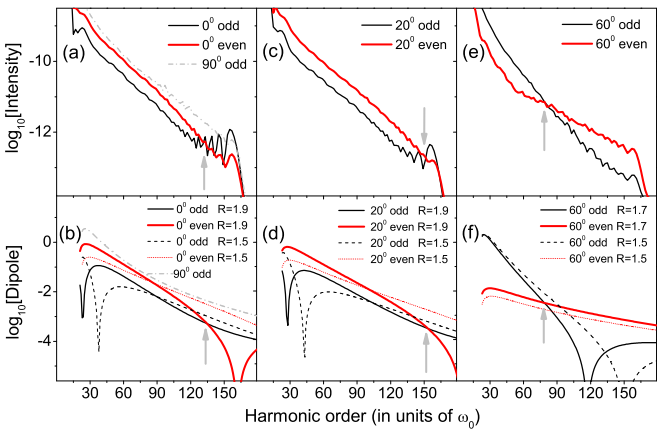

FIG. 7. Comparison of odd-even harmonic spectra (a), (c), (e) and dipoles $|D_{\rm odd\,(even)}(\omega,\theta)|^2$ (b), (d), (f) of HeH^+ for different angles θ. The dipoles are calculated using different internuclear distances R, as shown. The vertical arrows indicate the crossing points of odd-even spectra and dipoles.

$-\mathbf{R}_a|$, $r_b = |\mathbf{r} - \mathbf{R}_b|$, and $\kappa = \sqrt{2I_p}$. Z_1 and Z_2 are the effective charges for the He and H centers, respectively, $\mathbf{R}_a = Z_2\mathbf{R}/(Z_1 + Z_2)$ and $\mathbf{R}_b = -Z_1\mathbf{R}/(Z_1 + Z_2)$. $\mathbf{R}$ is the internuclear distance. N_f is the normalization factor and I_p is the ionization potential of the ground state. $\mathbf{p}_k$ is the effective momentum of the continuum state $|\mathbf{p}\rangle \propto |e^{i\mathbf{p}_k\cdot\mathbf{r}}\rangle$ with $p_k = |\mathbf{p}_k| = [2(I_P + E_p)]^{1/2}$ that considers the Coulomb acceleration [7]. $E_p = \omega - I_p$ is the energy of the continuum state $|\mathbf{p}\rangle$. The qualitative relation between the corresponding dipoles $D_{\text{odd (even)}}$ and spectra $S_{\parallel}^{\text{odd (even)}}$ along the laser polarization is [23]

$$S_{\parallel}^{\text{odd}}(\omega,\theta) \sim |a(\omega)D_{\text{odd}}(\omega,\theta)|^2, \omega = (2n+1)\omega_0;$$
$$S_{\parallel}^{\text{even}}(\omega,\theta) \sim |a(\omega)D_{\text{even}}(\omega,\theta)|^2, \omega = 2n\omega_0. \quad (22)$$

$a(\omega)$ is the spectral amplitude of the continuum electron which is not sensitive to the angle θ [7]. This above relation clearly shows that the emission of odd or even harmonics from the asymmetric molecule is closely related to the symmetry of the asymmetric molecular orbital.

For an angle θ, we calculate these dipoles $D_{\text{odd (even)}}$ using the distance R_m which is corresponding to the peak of the distribution $\zeta(R)$ as discussed in Fig. 6, and the equilibrium separation $R_e = 1.5$ a.u. Figure 7(a) plots the odd-even HHG spectra at $\theta = 0^\circ$. Here, one can observe that the even spectrum (bold curve) is stronger than the odd one (thin curve) for harmonic orders lower than H133, and the situation reverses for higher orders, resulting in a clear crossing point of the odd and even spectra around H133, as indicated by the vertical arrow. This crossing phenomenon of odd-even spectra is reproduced by the odd versus even dipoles calculated with $R = 1.9$ a.u. in Fig. 7(b), as shown by the solid curves. By comparison, this crossing phenomenon is absent in the odd-even dipoles with $R = 1.5$ a.u., as shown by the dashed and the dotted curves. At $\theta = 90^\circ$, the even harmonics disappear. In addition, the dipole is independent of R [19]. For comparison, in Fig. 7(a), we also show the HHG spectrum at $\theta = 90^\circ$ (dashed-dotted curve), which is close to the even spectrum of $\theta = 0^0$ for lower orders, and remarkably higher than that for higher orders near to the cutoff region. These characteristics are also reproduced by the dipole of $\theta = 90^\circ$ versus the even dipole of $\theta = 0^\circ$ with $R = 1.9$ a.u. in Fig. 7(b).

Figures 7(c) and 7(e) plot the odd-even spectra at $\theta = 20^\circ$ and 60°. In both cases, the odd versus even spectra show a clear crossing point, in agreement with the predictions of the relevant dipoles in Figs. 7(d) and 7(f) calculated with R_m. The dipole curves in Fig. 7(f) calculated using $R = 1.5$ a.u. also show the crossing, but the position of the crossing point shifts to higher orders in comparison with the odd-even spectra in Fig. 7(e). The close relation between the odd-even spectra and the relevant dipoles calculated with R_m also holds as incomplete orientation [20] is considered (see Sec. V B). These results imply that the HHG of the system at an angle θ predominately occurs around a critical distance R_m. The latter depends on the nuclear motion, and can be tracked from the odd-even HHG spectra by exploiting, for example, the crossing phenomenon of these spectra.

In Fig. 7, the odd dipoles also show some striking minima arising from two-center interference [41]. (The positions of the minima predicted with R_e are about 15 to 30 orders higher than those with R_m here.) The minima, relating to the molecular structure [7,23], are absent in the HHG spectra due to the contributions of different HHG channels arising from the symmetry breaking [40]. Below, we will show that the polarization measurement of odd-even harmonics [25] provides another approach for probing the nuclear motion.

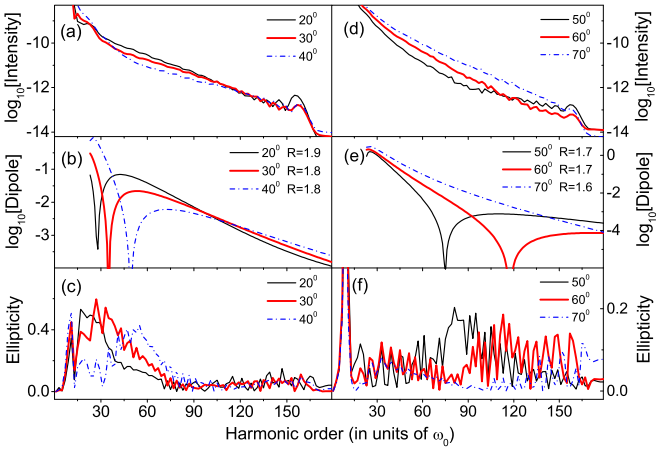

FIG. 8. Comparison of odd harmonic spectra (a), (d), dipoles $|D_{\text{odd}}(\omega,\theta)|^2$ (b), (e), and ellipticity of relevant harmonics (c), (f) for HeH^+ at different angles θ. The internuclear distances R used in the calculation of dipoles are as shown.

C. Ellipticity of odd-even harmonics

In Figs. 8(a) and 8(d), we show the odd spectra parallel to the laser polarization at different angles, averaged by the relevant ionization yields. We also compare them to the odd dipoles calculated with R_m in Figs. 8(b) and 8(e). The ellipticity of relevant harmonics is shown in Figs. 8(c) and 8(f). The ellipticity of HHG is determined by the amplitude ratio and the phase difference of the parallel and perpendicular harmonics. That is,

$$\varepsilon = \sqrt{\frac{1+\mu^2-\sqrt{1+2\mu^2\cos(2\delta)+\mu^4}}{1+\mu^2+\sqrt{1+2\mu^2\cos(2\delta)+\mu^4}}}, \quad (23)$$

where $\mu = S_\perp/S_\parallel$ and $\delta = \phi_\perp - \phi_\parallel$. The intensity and phase of the harmonic components are given by $S_{\parallel(\perp)} = |F_{\parallel(\perp)}(\omega)|^2$ and $\phi_{\parallel(\perp)}(\omega) = \arg[F_{\parallel(\perp)}(\omega)]$. The range of the ellipticity is $0 \leqslant \varepsilon \leqslant 1$. The linear, elliptical, and circular polarizations correspond to $\varepsilon = 0$, $0 < \varepsilon < 1$, and $\varepsilon = 1$, respectively.

One can observe, from Figs. 8(b) and 8(e), the minimum in the dipoles shifts towards higher harmonic orders as the angle increases. When the minimum in the corresponding spectra in Figs. 8(a) and 8(d) does not appear, the maximal ellipticity of harmonics appears at the harmonic order that corresponds to the position of the minimum in the dipole, as shown in Figs. 8(c) and 8(f). These results are similar to the fixed-nuclei cases [25]. They reveal that for the vibrating system, the minimum in the dipole can still be probed through the measurement of the ellipticity of harmonics. Since the minimum is associated with the molecular symmetry and the critical distance R_m here, the probe of the minimum amounts to the probe of the nuclear motion and the molecular structure.

We note that the odd spectra at larger angles, as shown in Fig. 8(d), also show the striking crossing phenomenon, consistent with the predictions of the relevant dipoles in Fig. 8(e). Results discussed in the paper have been checked at other laser parameters, such as $I = 2 \times 10^{15}$ W/cm^2 and $\lambda = 500$ nm. Extended simulations also show that the distance R_m is independent of θ for the symmetric case of H_2 (see Sec. V C).

V. EXTENDED DISCUSSIONS ON MULTIELECTRON EFFECTS, ORIENTATION EFFECTS, AND SYMMETRIC CASES

In this section, we check our main results with using other laser parameters, using a 1D two-electron model for HeH^+ and considering incomplete orientation of the asymmetric molecule. To understand the angle dependence of the critical distance R_m for HeH^+, we also show the results for the HHG from vibrating H_2.

A. Other laser parameters and multielectron effects on nuclear dynamics

In Fig. 3(a), it has been shown that the lowest vibrational state $|0\rangle$ of the system depletes fast, resulting in the rapid spreading of the nuclear wave packet. This depletion is asymmetric in one laser cycle. Using a two-level model, it has been shown that the asymmetric depletion arises from the effect of the permanent dipole which induces a strong coupling between the two lowest vibrational states of the system. The effect of the permanent dipole is associated with the laser intensity. From the two-level model in Sec. III B, one can predict that at lower laser intensities, the permanent dipole plays a relatively smaller role and the coupling between these two states is also weaker. This prediction agrees with our extended simulations shown in Fig. 9(a) with $I = 1.5 \times 10^{15}$ W/cm^2. Here, the depletion of the $|0\rangle$ state is slower in comparison with the high-intensity case in Fig. 3(a). But, this asymmetric-depletion phenomenon in one laser cycle can still be clearly identified here.

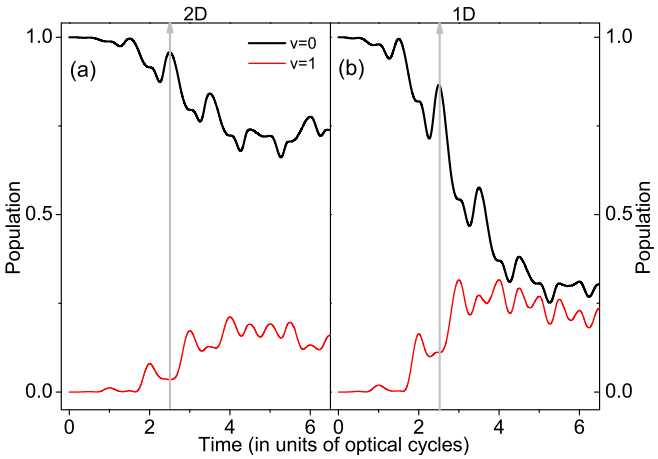

FIG. 9. Time-dependent populations of the two lowest vibrational states of HeH^+ at $\theta = 0^\circ$ obtained with different approaches: (a) the approach for a 2D electron with the effective potential $V_{\rm eff}$ introduced in Sec. II at $I = 1.5 \times 10^{15}$ W/cm^2 and $\lambda = 600$ nm; (b) the approach for two 1D electrons with $I = 1 \times 10^{15}$ W/cm^2 and $\lambda = 600$ nm.

This quick-asymmetric depletion of the lowest vibrational state relating to the quick spreading of the nuclear wave packet is also verified with the use of a 1D two-electron model for HeH^+ in a non-BO approach. The 1D Hamiltonian is [30] (in atomic units)

$$H(t) = -\frac{1}{2\mu_N}\frac{\partial^2}{\partial R^2} + \frac{(Z_1 Z_2)}{R} + \frac{1}{\sqrt{(x_1 - x_2)^2 + \varepsilon}} + \sum_{j=1}^{2}\left[-\frac{1}{2\mu_e}\frac{\partial^2}{\partial x_j^2} + V_{en}(R, x_j) + x_j E(t)\right] + V_n, \tag{24}$$

where $\mu_N = M_{\rm He}M_{\rm H}/(M_{\rm He} + M_{\rm H})$ is the nuclear reduced mass, $M_{\rm He}$ and $M_{\rm H}$ are masses of He and H nuclei. $\mu_e = (M_{\rm He} + M_{\rm H})/(M_{\rm He} + M_{\rm H} + 1)$ is the electronic reduced mass. R is the internuclear separation and x_j is the electronic coordinate. The potential V_{en}, describing the interaction between the electron and the nuclei, has the following form:

$$V_{en}(R, x) = -\frac{Z_1}{\sqrt{(x - R_1)^2 + \varepsilon}} - \frac{Z_2}{\sqrt{(x - R_2)^2 + \varepsilon}}. \tag{25}$$

Here, $Z_1 = 2$ and $Z_2 = 1$ are the charges for the He and H centers, respectively. R_1 and R_2 are the positions of the He and H nuclei with $R_1 = M_{\rm H}R/(M_{\rm He} + M_{\rm H})$ and $R_2 = -M_{\rm He}R/(M_{\rm He} + M_{\rm H})$. $\varepsilon = 0.59$ is the softening parameter, which is adjusted such that the ground-state energy of the model HeH^+ molecule matches the real one of $E_0 = -2.98$ a.u. The term $V_n \equiv V_n(R, t)$ is the laser-nuclei-interaction term, as defined in Sec. II. We mention that the equilibrium separation of the model molecule is $R = 2$ a.u. here, somewhat larger than the real one of $R = 1.4$ a.u. As the 1D model molecule with a larger equilibrium separation is easier to ionize than the 2D one, in the 1D TDSE, we use the laser parameters of $I = 1 \times 10^{15}$ W/cm^2 and $\lambda = 600$ nm. The 1D results for the populations of these two lowest vibrational states are presented in Fig. 9(b), which are similar to the 2D ones with showing the quick-asymmetric depletion of the $|0\rangle$ state in one laser cycle and a large population of the $|1\rangle$ state at $t > 1.5T$.

The 1D two-electron model of Eq. (24) considers the multielectron effect with the reduction of the dimension of the electron motion, when the 2D single-electron model of Eq. (1) allows one to consider the orientation of the system with the omission of the electron-electron correlation. This similarity between the 1D and 2D results here indeed implies that the rapid-asymmetric depletion of the ground state is not sensitive to the dimension of the system and is mostly relevant to the single-electron dynamics. As discussed in Sec. III B, we anticipate that the effect of the permanent dipole associated with single-electron dynamics is mainly responsible for the rapid depletion.

B. Orientation effects on odd-even HHG

The molecules are not perfectly oriented in experiments [20]. To study the influence of incomplete orientation, one

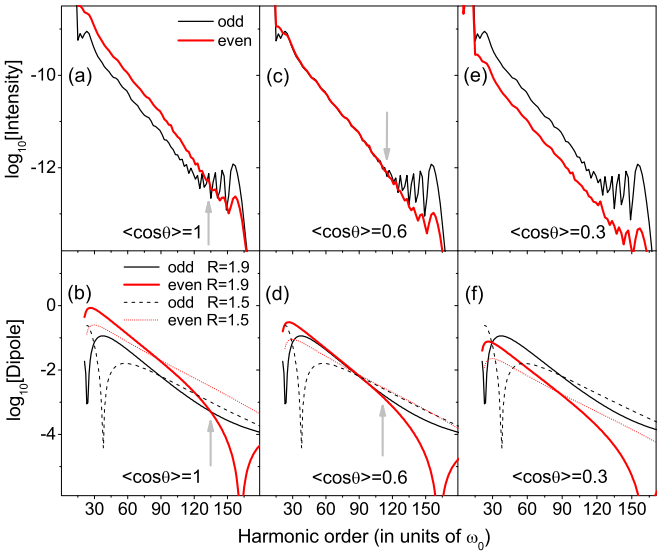

FIG. 10. Comparison of odd-even harmonic spectra (a), (c), (e) and dipoles $|D_{\text{odd (even)}}(\omega,\theta)|^2$ (b), (d), (f) of HeH^+ at $\theta = 0^\circ$ for different degrees of orientation $\langle\cos\theta\rangle$. The dipoles are calculated using different internuclear distances R, as shown. The vertical arrows indicate the crossing points of odd-even spectra and dipoles. The laser intensity used here is $I = 2.5 \times 10^{15}$ W/cm^2 and the laser wavelength is $\lambda = 600$ nm.

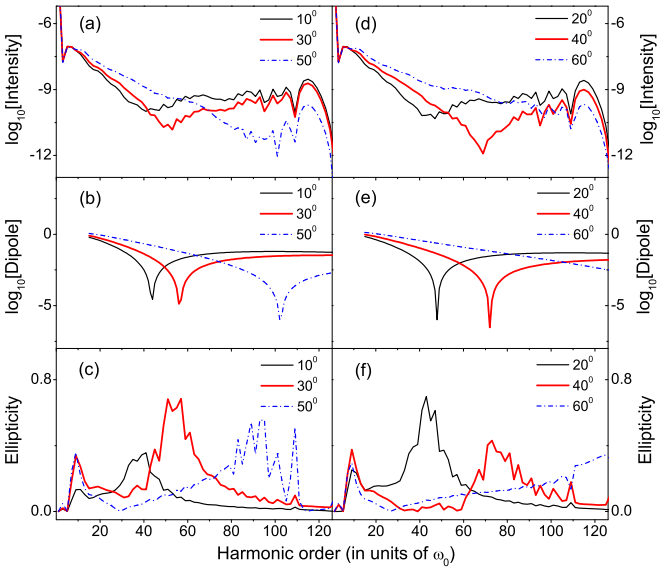

FIG. 11. Comparison of odd harmonic spectra (a), (d), dipoles $|D_{\text{odd}}(\omega,\theta)|^2$ (b), (e), and ellipticity of relevant harmonics (c), (f) for H_2 at different angles θ. The dipoles are calculated with the same internuclear distance $R = 1.6$ a.u. The laser intensity used here is $I = 4 \times 10^{14}$ W/cm^2 and the laser wavelength is $\lambda = 1000$ nm.

can assume that the molecules are perfectly aligned and only partially oriented (with n_u molecules pointing up and n_d pointing down). Then, the degree of orientation can be defined as

$$\langle\cos\theta\rangle = (n_u - n_d)/(n_u + n_d). \tag{26}$$

We have calculated the odd-even HHG spectra of HeH^+ and the corresponding dipoles for different degrees of orientation at different angles θ. Some typical results at $\theta = 0^\circ$ are presented in Fig. 10. One can observe from Fig. 10, as the yields of odd harmonics depend only on the alignment of the ensemble, the yields of even harmonics are sensitive to the orientation and decrease with the decrease of the degree of orientation. However, in all cases, the relative yields of odd versus even harmonics are well described by the odd versus even dipoles calculated with the critical distance $R_m = 1.9$ a.u. These results imply that as incomplete orientation is considered, the vibrational motion of the nuclei can still be read from the odd versus even HHG spectra.

In practice, the alignment of the sample is also incomplete and the highest degree of molecular alignment can be around 0.8. In this situation, our results in Fig. 10 indicate that for a better estimation of the nuclear motion using the phenomena associated with odd-even HHG spectra such as the crossing phenomenon of these spectra, a high degree of orientation is preferred. As the high degree of orientation is not easy to achieve in present experiments, the ellipticity measurement of the odd spectra discussed in Fig. 8 may be a preferable approach for probing the nuclear motion since the odd spectra are only dependent of the alignment of the ensemble.

C. Comparison with symmetric cases of H_2

For symmetric molecules such as H_2, the even harmonics are absent. In addition, the effect of the permanent dipole disappears and the vibrational motion of the molecule is not sensitive to the angle θ. In the situation, the value of R_m is independent of the angle θ and is usually nearer to R_e than in the asymmetric case, as shown in Fig. 11.

The results in Fig. 11 for vibrating H_2 are obtained with similar numerical procedures and similar laser pulses to the case of HeH^+ introduced in Secs. II– IV. As one can see here, for different orientation angles θ, the behaviors of the spectra, especially for the positions of the minima arising from two-center interference, agree with the predictions of the dipoles $D_{\text{odd}}(\omega,\theta)$ obtained with the same distance $R_m = 1.6$ a.u. This distance is near to the equilibrium separation of H_2 ($R_e = 1.4$ a.u.), implying the slower nuclear dynamics of H_2 in comparison with HeH^+.

One can also observe from Fig. 11, at the harmonic order corresponding to the position of the minimum in the dipoles, the ellipticity of harmonics shows a maximum, similar to the asymmetric case of HeH^+. The results also support our conclusion in the paper that the polarization measurement of harmonics can be used as a tool to probe the instantaneous structure of the vibrating system.

Before conclusion, we add that aside from the omission of the rotational motion of the nuclei which is important in a long pulse, another limitation of our discussions in the paper is the omission of the macroscopic propagation of both fundamental and harmonic fields. This macroscopic propagation can result in the phase mismatch of HHG which remarkably reduces the HHG yield and therefore influences the use of HHG as a tool to probe the nuclear dynamics. To diminish the phase mismatch, in real experiments, short laser pulses with long laser wavelengths and moderate laser

intensities at which the ionization of the sample is weak are preferred [42,43].

VI. CONCLUSION

In summary, we have studied the electron-nuclear coupled dynamics of the vibrating HeH^+ system in few-cycle laser pulses. Our simulations show that the nuclear wave packet of the asymmetric system spreads rapidly at small orientation angles. This spreading remarkably influences the HHG. It leads to the occurrence of the HHG around a critical distance R_m beyond the equilibrium geometry. This distance R_m reflects the spreading extent of the nuclear wave packet. It depends on the molecular orientation and can be tracked from the spectra and ellipticity of odd-even harmonics. By contrast, the HHG for H_2 occurs at a distance near to the equilibrium separation and this distance is not sensitive to the molecular orientation. We show that the permanent dipole of the HeH^+ system (which is absent for H_2) plays an important role in the electron-nuclear coupled dynamics of the asymmetric system. The interaction of the laser field and the permanent dipole provides an effective approach for transferring the populations from the ground state to the excited vibrational states, resulting in the fast nuclear dynamics. As the effect of the permanent dipole depends on the molecular orientation, the nuclear dynamics activated by the effect such as the fast spreading of the nuclear wave packet does so.

When the ionization of the electron prefers to occur at larger internuclear distances [38,39] at which the energy gap between the ground state and the first excited state of the electron is smaller and the effect of the permanent dipole is stronger, the rapid spreading of the nuclear wave packet will influence the asymmetric ionization [26] and the excited-state dynamics [33] of the asymmetric system. It is possible to probe these influences of this spreading on ionization with elliptically polarized pulses [3,44] or attosecond extreme ultraviolet pulses [45]. In particular, when the excited-state channel is activated, the tunneling time and the tunneling position of the electron will be affected [46]. This spreading, therefore, can add new observables into the attoclock experiment [47,48] which probes the tunneling time delay of ionization. Due to the influence on single ionization, this effect is also expected to contribute to nonsequential double ionization [49–51] of the asymmetric system.

ACKNOWLEDGMENTS

This work was supported by the National Natural Science Foundation of China (Grant No. 11274090) and the Fundamental Research Funds for the Central Universities (Grant No. SNNU. GK201403002).

[1] P. B. Corkum and F. Krausz, Nat. Phys. **3**, 381 (2007).
[2] F. Lépine, M. Y. Ivanov, and M. J. J. Vrakking, Nat. Photonics **8**, 195 (2014).
[3] Hiromichi Niikura, F. Légaré, R. Hasbani, A. D. Bandrauk, M. Yu. Ivanov, D. M. Villeneuve, and P. B. Corkum, Nature (London) **417**, 917 (2002).
[4] P. Eckle, A. N. Pfeiffer, C. Cirelli, A. Staudte, R. Dörner, H. G. Muller, M. Büttiker, and U. Keller, Science **322**, 1525 (2008).
[5] P. B. Corkum, Phys. Rev. Lett. **71**, 1994 (1993).
[6] P. Salieres, B. Carre, L. Le Deroff, F. Grasbon, G. G. Paulus, H. Walther, R. Kopold, W. Becker, D. B. Milosevic, A. Sanpera, and M. Lewenstein, Science **292**, 902 (2001).
[7] J. Itatani, J. Levesque, D. Zeidler Hiromichi Niikura, H. Pepin, J. C. Kieffer, P. B. Corkum, and D. M. Villeneuve, Nature (London) **432**, 867 (2004).
[8] V.-H. Le, A.-T. Le, R.-H. Xie, and C. D. Lin, Phys. Rev. A **76**, 013414 (2007).
[9] C. Vozzi, M. Negro, F. Calegari, G. Sansone, M. Nisoli, S. De Silvestri, and S. Stagira, Nat. Phys. **7**, 822 (2011).
[10] O. Smirnova, Y. Mairesse, S. Patchkovskii, N. Dudovich, D. Villeneuve, P. Corkum, and M. Yu. Ivanov, Nature (London) **460**, 972 (2009).
[11] D. Shafir, H. Soifer, B. D. Bruner, M. Dagan, Y. Mairesse, S. Patchkovskii, M. Yu. Ivanov, O. Smirnova, and N. Dudovich, Nature (London) **485**, 343 (2012).
[12] M. Lein, Phys. Rev. Lett. **94**, 053004 (2005).
[13] S. Baker, J. S. Robinson, C. A. Haworth, H. Teng, R. A. Smith, C. C. Chirilă, M. Lein, J. W. G. Tisch, and J. P. Marangos, Science **312**, 424 (2006).
[14] H. J. Wörner, J. B. Bertrand, D. V. Kartashov, P. B. Corkum, and D. M. Villeneuve, Nature (London) **466**, 604 (2010).
[15] P. M. Kraus, B. Mignolet, D. Baykusheva, A. Rupenyan, L. Horný, E. F. Penka, G. Grassi, O. I. Tolstikhin, J. Schneider, F. Jensen, L. B. Madsen, A. D. Bandrauk, F. Remacle, and H. J. Wörner, Science **350**, 790 (2015).
[16] X. B. Bian and A. D. Bandrauk, Phys. Rev. Lett. **105**, 093903 (2010).
[17] A. Etches, M. B. Gaarde, and L. B. Madsen, Phys. Rev. A **84**, 023418 (2011).
[18] J. Heslar, D. Telnov, and S.-I. Chu, Phys. Rev. A **83**, 043414 (2011).
[19] Y. Chen and B. Zhang, Phys. Rev. A **84**, 053402 (2011).
[20] E. Frumker, C. T. Hebeisen, N. Kajumba, J. B. Bertrand, H. J. Wörner, M. Spanner, D. M. Villeneuve, A. Naumov, and P. B. Corkum, Phys. Rev. Lett. **109**, 113901 (2012).
[21] P. M. Kraus, A. Rupenyan, and H. J. Wörner, Phys. Rev. Lett. **109**, 233903 (2012).
[22] E. Frumker, N. Kajumba, J. B. Bertrand, H. J. Wörner, C. T. Hebeisen, P. Hockett, M. Spanner, S. Patchkovskii, G. G. Paulus, D. M. Villeneuve, A. Naumov, and P. B. Corkum, Phys. Rev. Lett. **109**, 233904 (2012).
[23] Y. J. Chen, L. B. Fu, and J. Liu, Phys. Rev. Lett. **111**, 073902 (2013).
[24] P. M. Kraus, D. Baykusheva, and H. J. Wörner, Phys. Rev. Lett. **113**, 023001 (2014).
[25] S. Yu, B. Zhang, Y. Li, S. Yang, and Y. Chen, Phys. Rev. A **90**, 053844 (2014).

[26] G. L. Kamta and A. D. Bandrauk, Phys. Rev. Lett. **94**, 203003 (2005).
[27] A. Etches and L. B. Madsen, J. Phys. B: At., Mol. Opt. Phys. **43**, 155602 (2010).
[28] X. Y. Miao and H. N. Du, Phys. Rev. A **87**, 053403 (2013).
[29] H. B. Pedersen, S. Altevogt, B. Jordon-Thaden, O. Heber, M. L. Rappaport, D. Schwalm, J. Ullrich, D. Zajfman, R. Treusch, N. Guerassimova, M. Martins, J.-T. Hoeft, M. Wellhöfer, and A. Wolf, Phys. Rev. Lett. **98**, 223202 (2007).
[30] John R. Hiskes, Phys. Rev. **122**, 1207 (1961).
[31] T. A. Green, H. H. Michels, J. C. Browne, and M. M. Madsen, J. Chem. Phys. **61**, 5186 (1974).
[32] M. D. Feit, J. A. Fleck, Jr., and A. Steiger, J. Comput. Phys. **47**, 412 (1982).
[33] Y. Chen and B. Zhang, Phys. Rev. A **86**, 023415 (2012).
[34] M. Lein, T. Kreibich, E. K. U. Gross, and V. Engel, Phys. Rev. A **65**, 033403 (2002).
[35] A. Picón, J. Biegert, A. Jaron-Becker, and A. Becker, Phys. Rev. A **83**, 023412 (2011).
[36] A. Picón, A. Jaron-Becker, and A. Becker, Phys. Rev. Lett. **109**, 163002 (2012).
[37] X. M. Tong, S. Watahiki, K. Hino, and N. Toshima, Phys. Rev. Lett. **99**, 093001 (2007).
[38] T. Seideman, M. Yu. Ivanov, and P. B. Corkum, Phys. Rev. Lett. **75**, 2819 (1995).
[39] T. Zuo and A. D. Bandrauk, Phys. Rev. A **52**, R2511 (1995).
[40] B. Zhang, Y. Chen, X. Jiang, and X. Sun, Phys. Rev. A **88**, 053428 (2013).
[41] M. Lein, N. Hay, R. Velotta, J. P. Marangos, and P. L. Knight, Phys. Rev. Lett. **88**, 183903 (2002).
[42] V. S. Yakovlev, M. Ivanov, and F. Krausz, Opt. Express **15**, 15351 (2007).
[43] M.-C. Chen, P. Arpin, T. Popmintchev, M. Gerrity, B. Zhang, M. Seaberg, D. Popmintchev, M. M. Murnane, and H. C. Kapteyn, Phys. Rev. Lett. **105**, 173901 (2010).
[44] R. Boge, C. Cirelli, A. S. Landsman, S. Heuser, A. Ludwig, J. Maurer, M. Weger, L. Gallmann, and U. Keller, Phys. Rev. Lett. **111**, 103003 (2013).
[45] S. X. Hu, L. A. Collins, and B. I. Schneider, Phys. Rev. A **80**, 023426 (2009).
[46] M. Klaiber, K. Z. Hatsagortsyan, and C. H. Keitel, Phys. Rev. Lett. **114**, 083001 (2015).
[47] P. Eckle, M. Smolarski, F. Schlup, J. Biegert, A. Staudte, M. Schöffler, H. G. Muller, R. Dörner, and U. Keller, Nat. Phys. **4**, 565 (2008).
[48] A. N. Pfeiffer, C. Cirelli, M. Smolarski, D. Dimitrovski, M. Abu-samha, L. B. Madsen, and U. Keller, Nat. Phys. **8**, 76 (2012).
[49] H. Niikura, F. Légaré, R. Hasbani Misha, Yu. Ivanov, D. M. Villeneuve, and P. B. Corkum, Nature (London) **421**, 826 (2003).
[50] D. Zeidler, A. Staudte, A. B. Bardon, D. M. Villeneuve, R. Dörner, and P. B. Corkum, Phys. Rev. Lett. **95**, 203003 (2005).
[51] W. Becker, X. Liu, P. J. Ho, and J. H. Eberly, Rev. Mod. Phys. **84**, 1011 (2012).